

pubs.acs.org/JACS Article

## Structure and Site Evolution of Framework Ni Species in MIL-127 MOFs for Propylene Oligomerization Catalysis

Benjamin Yeh, Saumil Chheda, Steven D. Prinslow, Adam S. Hoffman, Jiyun Hong, Jorge E. Perez-Aguilar, Simon R. Bare, Connie C. Lu, Laura Gagliardi, and Aditya Bhan\*



Cite This: J. Am. Chem. Soc. 2023, 145, 3408-3418



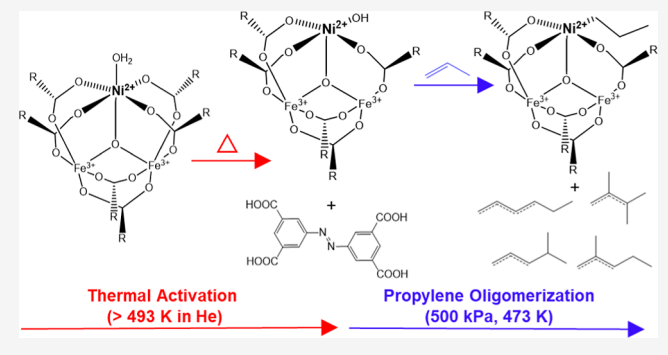
**ACCESS** I

III Metrics & More

Article Recommendations

s Supporting Information

**ABSTRACT:** A mixed-valence oxotrimer metal—organic framework (MOF), Ni-MIL-127, with a fully coordinated nickel atom and two iron atoms in the inorganic node, generates a missing linker defect upon thermal treatment in helium (>473 K) to engender an open coordination site on nickel which catalyzes propylene oligomerization devoid of any cocatalysts or initiators. This catalyst is stable for  $\sim$ 20 h on stream at 500 kPa and 473 K, unprecedented for this chemistry. The number of missing linkers on synthesized and activated Ni-MIL-127 MOFs is quantified using temperature-programmed oxidation,  $^1{\rm H}$  nuclear magnetic resonance spectroscopy, and X-ray absorption spectroscopy to be  $\sim$ 0.7 missing linkers per nickel; thus, a majority of Ni species in the



MOF framework catalyze propylene oligomerization. In situ NO titrations under reaction conditions enumerate ~62% of the nickel atoms as catalytically relevant to validate the defect density upon thermal treatment. Propylene oligomerization rates on Ni-MIL-127 measured at steady state have activation energies of 55–67 kJ mol<sup>-1</sup> from 448 to 493 K and are first-order in propylene pressures from 5 to 550 kPa. Density functional theory calculations on cluster models of Ni-MIL-127 are employed to validate the plausibility of the missing linker defect and the Cossee—Arlman mechanism for propylene oligomerization through comparisons between apparent activation energies from steady-state kinetics and computation. This study illustrates how MOF precatalysts engender defective Ni species which exhibit reactivity and stability characteristics that are distinct and can be engineered to improve catalytic activity for olefin oligomerization.

#### ■ INTRODUCTION

Metal-organic frameworks (MOFs) contain a variety of structural defects which can be beneficial for catalysis. 1-5 These defects can be engendered from missing linkers in the framework to expose relevant catalytic active sites and can be tuned based on the choice of modulators used in synthesis to change the electronic properties of the catalytic site. 4,6-8 UiO-66 and NU-1000, zirconium-oxide based MOFs, for example, have been shown to facilitate cyclization of (+)-citronellal to isopulegol and epoxide-ring opening reactions, respectively, through a coordinately unsaturated zirconium Lewis acid site derived from a missing linker defect. 9,10 Up to 25% of linkers can be missing in UiO-66 to generate these unsaturated zirconium Lewis acid sites. 11 The strength of coordinately unsaturated zirconium Lewis acid sites on UiO-66 can be tuned by the choice of acetic acid, formic acid, difluoroacetic acid, or trifluoroacetic acid modulators in synthesis while maintaining the structure of the MOF as these modulators have similar chemical functionalities as the organic linker.<sup>8,12</sup> Thermal treatment of MOF-5, a zinc-based MOF, below its decomposition temperature exposes zinc sites through partial decomposition of the bridging carboxylate in the organic

linker.<sup>13</sup> Iron oxotrimer MOF catalysts, such as MIL-100 and PCN-250/MIL-127, have been proposed to develop an unsaturated Fe(II) site from a saturated Fe(III) through the loss of an OH species or a decarboxylation mechanism to lose CO<sub>2</sub> on the organic linker to expose relevant catalytic sites for alkane oxidation reactions after thermal activation.<sup>7,14,15</sup> Missing linker defects and the coordination environment of unsaturated metal sites in MOFs have been probed using techniques such as thermogravimetric analysis (TGA), <sup>1</sup>H nuclear magnetic resonance (NMR) spectroscopy, and X-ray absorption spectroscopy (XAS).<sup>1,11,12,16</sup> Metal centers can be exposed for their respective chemistry upon generation of a missing linker defect, but a major challenge in MOF catalysis involves identifying and quantifying relevant open coordina-

Received: October 4, 2022 Published: February 1, 2023





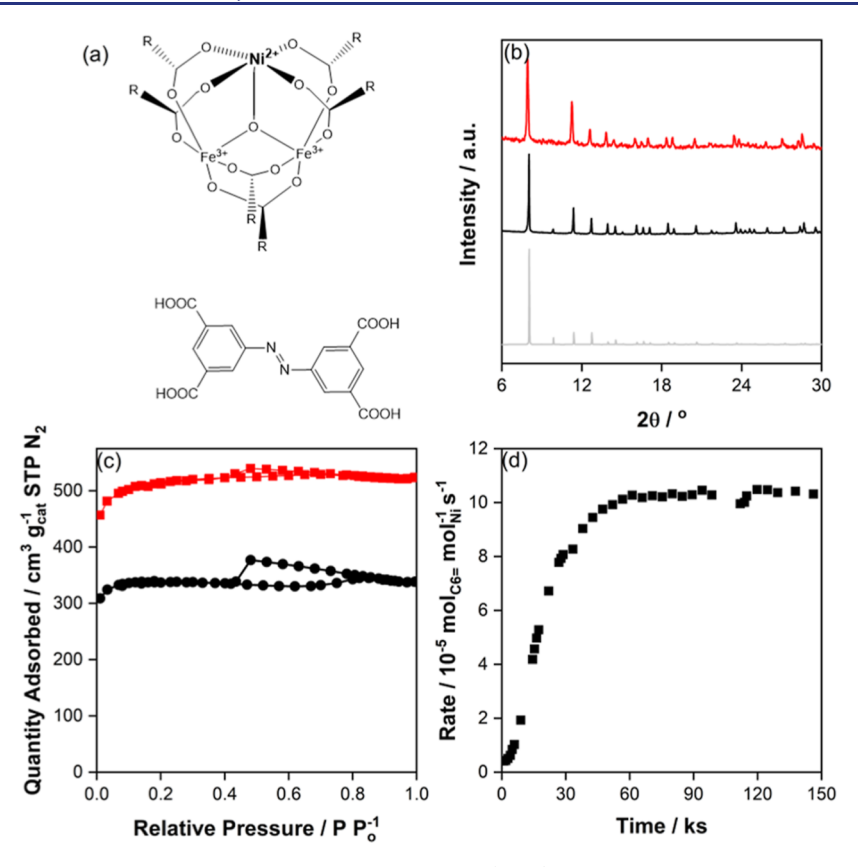


Figure 1. (a) Modular building blocks for Ni-MIL-127 consisting of  $[Fe_2Ni(\mu_3-O)]$  nodes and 3,3′,5,5′-azobenzenetetracarboxylate (ABTC) linkers. (b) PXRD for computed (gray), as-synthesized (black), and thermally treated (red) structures of Ni-MIL-127 and (c)  $N_2$  isotherms for Ni-MIL-127 as-synthesized (black) and after thermal treatment (red). (d) Time on stream for propylene oligomerization at 0.83 cm<sup>3</sup> s<sup>-1</sup> propylene at 500 kPa and 473 K on 26.3 mg Ni-MIL-127.

tion catalytic sites from the formation of defects as nonuniformities exist in the MOF structure.<sup>1</sup>

An open coordination site is purportedly required to facilitate the Cossee-Arlman mechanism for olefin oligomerization on nickel-based catalysts after the reactant olefin molecule binds to a vacant nickel site to undergo a stoichiometric reaction to generate nickel-alkyl or nickelhydride species. <sup>17–25</sup> Heterogeneous nickel-zeolite catalysts for propylene oligomerization such as Ni–Na–X, <sup>26</sup> Ni–SiO<sub>2</sub>, <sup>26</sup> Ni-Na-MOR,<sup>26</sup> and Ni-M-MCM-41<sup>27</sup> inherently have an open coordination site but deactivate with time on stream at elevated temperatures. Nickel-framework MOF catalysts for propylene oligomerization such as Ni-MOF-74<sup>28</sup> are proposed to generate a Ni-propyl species during the induction period through the loss of a Ni-O ligand and deactivate with time on stream, while Ni-MFU-4l<sup>29</sup> inherently has an open coordination site but uses cocatalysts to promote propylene oligomerization. Due to the lack of catalyst stability for propylene oligomerization on these materials, few reports elucidate either the mechanism or the kinetics devoid of deactivation for this chemistry, while the Cossee-Arlman mechanism has been proposed for ethylene oligomerization on nickel catalysts.17-

Herein, we report a stable trimeric bimetallic Ni-MIL-127 MOF, with a fully coordinated nickel atom and two iron atoms in the inorganic node as-synthesized, which engenders a coordinately unsaturated nickel site upon thermal treatment (493 K) in flowing helium through the loss of a linker, as determined from temperature-programmed oxidation (TPO), <sup>1</sup>H NMR spectroscopy, and XAS. Upon thermal treatment, the

catalyst undergoes an induction period and oligomerizes propylene in the absence of activators and cocatalysts and is stable for ~1000 min on stream, distinct from other catalysts for this chemistry. The Cossee-Arlman mechanism for propylene oligomerization is affirmed by comparisons of apparent activation enthalpies through steady-state kinetic measurements and density functional theory (DFT) calculations on cluster models of Ni-MIL-127 to contend that light olefin oligomerization occurs via the Cossee-Arlman mechanism regardless of the length and carbon number of the reacting linear olefin. Our investigation of Ni-MIL-127 highlights that as-synthesized MOF materials can be precatalysts that generate defects to engender active sites for catalysis and allows us to formulate catalysts with isolated metal centers with varying coordination and electronic structure environments that can be probed and tuned through a combination of experiment and computation.

#### ■ RESULTS AND DISCUSSION

Ni-MIL-127 is a mixed-metal MOF consisting of  $[Fe_2Ni(\mu_3-O)]$  nodes and 3,3′,5,5′-azobenzenetetracarboxylate (ABTC) linkers (Figure 1a). Powder X-ray diffraction (PXRD) and nitrogen isotherms, shown in Figure 1b and 1c, respectively, were used to confirm the crystallinity and porosity of the assynthesized material. Mössbauer spectra (Figure S3) acquired at 25 K affirm that the iron species are Fe(III) in assynthesized samples, and scanning electron microscopy—energy-dispersive spectroscopy (SEM-EDS) was conducted

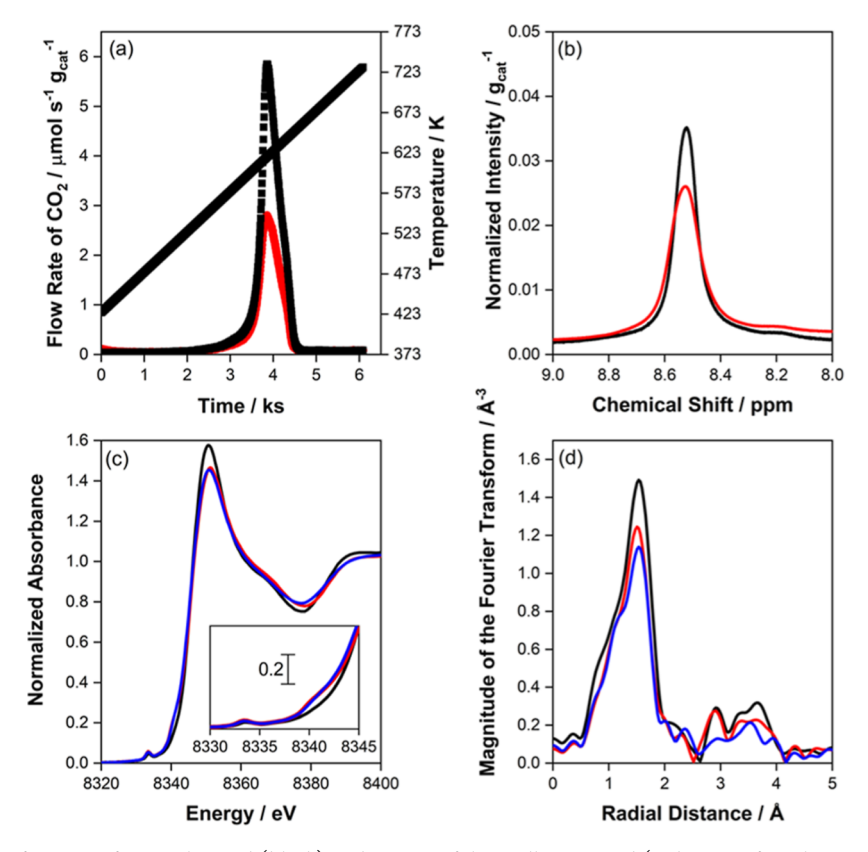


Figure 2. (a) TPO profile of 4.6 mg of as-synthesized (black) and 3.7 mg of thermally activated (red, 493 K for 4 h in 0.83 cm<sup>3</sup> s<sup>-1</sup> of He) Ni-MIL-127, outlining the evolution of CO<sub>2</sub> with the temperature ramped at 0.05 K s<sup>-1</sup> in 0.83 cm<sup>3</sup> s<sup>-1</sup> He, 0.17 cm<sup>3</sup> s<sup>-1</sup> Ar, and 0.17 cm<sup>3</sup> s<sup>-1</sup> O<sub>2</sub>. (b)  $^{1}$ H NMR spectra for 23.2 mg of as-synthesized (black) and 17.2 mg of thermally activated (red, 493 K for 4 h in 0.83 cm<sup>3</sup> s<sup>-1</sup> of He) Ni-MIL-127 in 1 M NH<sub>4</sub>OH/D<sub>2</sub>O normalized to 100  $\mu$ L of acetonitrile. (c) Ni K-edge XANES, with the inset showing the pre-edge peaks, and (d) EXAFS data [magnitude of the Fourier transform ( $k^2$ -weight)] in the k range of 3.0 Å<sup>-1</sup> < k < 13.0 Å<sup>-1</sup> for Ni-MIL-127 as-synthesized (black) and thermally activated (513 K in 0.25 cm<sup>3</sup> s<sup>-1</sup> helium, red) at a steady state (ambient pressure of 0.14 cm<sup>3</sup> s<sup>-1</sup> propylene at 513 K after 10 h, blue).

to determine the nickel-to-iron ratio, which was 1:2.7 (Figure S2, Table S2, and eq S2).

Reactivity, Structure, and Active Sites of Ni-MIL-127 for Propylene Oligomerization. After thermally activating Ni-MIL-127 in 0.83 cm $^{3}$  s $^{-1}$  of helium at 493 K (0.05 K s $^{-1}$ ) for 4 h, the catalytic behavior of the material was examined for propylene oligomerization in 0.83 cm<sup>3</sup> s<sup>-1</sup> propylene at 500 kPa and 473 K in the absence of activators, as shown in Figure 1d. As a reference, the pure iron trimer MIL-127 material was tested for propylene oligomerization under the same process conditions to reveal hexene formation rates 3 orders of magnitude lower than Ni-MIL-127, as shown in Figure S13. Similar to other olefin oligomerization systems on heterogeneous catalysts devoid of cocatalysts and activators, an induction period (~60 ks) is observed<sup>26,32</sup> on Ni-MIL-127 and has been attributed to the formation of the catalytically relevant surface species for oligomerization. 17,18,21,22 We note that Ni-MIL-127 is stable for propylene oligomerization after the induction period for another ~60 ks, which is unprecedented for propylene oligomerization on heterogeneous catalysts at elevated temperatures and pressures. Stable propylene oligomerization rates were obtained on Ni-Al-MCM-41 but at subambient temperatures.<sup>23</sup> Prior work on Ni-Na-X shows stable propylene oligomerization rates after the catalyst is activated in 500 kPa of propylene at 493 K and the temperature is subsequently decreased to 393-453 K; however, the catalyst deactivates at 453 and 493 K without prior activation.<sup>26</sup> The Ni-MIL-127 system for propylene

oligomerization reported herein showcases a Ni-based catalyst that is stable at elevated temperatures without prior exposure to propylene. Our disquisition examines how framework atoms in Ni-MIL-127 enable site isolation and provide opportunities to tailor unique coordination and electronic environments to enhance oligomerization reactivity. A comparison of heterogeneous nickel catalysts for propylene oligomerization and their respective turnover frequencies and linear hexene selectivities is reported in Table S7.

Olefin oligomerization on heterogeneous nickel catalysts requires an open coordination site to bind a gas-phase olefin molecule, as noted on Ni-Na-X<sup>26</sup> and Ni-SSZ-24<sup>21</sup> for propylene and ethylene oligomerization, respectively.<sup>20</sup> We sought to explain the reactivity of Ni-MIL-127 for propylene oligomerization as nickel on Ni-MIL-127 appears to be fully coordinated with four ABTC linkers, a bridging oxo species, and an aqua ligand. 30,33 Prior work on PCN-250/MIL-127 and their bimetallic analogues has shown that these materials undergo decarboxylation to open a coordination site on Fe(II) or M(II), as evinced by thermogravimetric analysis-mass spectrometry after thermal treatment. 7,33 These studies focused on the nature of the iron species, determined by <sup>57</sup>Fe Mössbauer and Fe K-edge XAS but do not investigate the nature of M(II) species. 7,33 Because nickel is the active species for propylene oligomerization as opposed to iron (Figure S13), we sought to quantify the number of missing linkers in both assynthesized and thermally treated (493 K in 0.83 cm<sup>3</sup> s<sup>-1</sup> helium for 4 h) samples to determine the fraction of missing

Scheme 1. Proposed Ni-MIL-127 Structures upon Thermal Treatment in Helium, Where Ph-COOH Is an ABTC Linker

$$\begin{array}{c} \text{R} \\ \text{$$

linkers on these samples and the effect they have on nickel active sites for propylene oligomerization.

TPO enumerates the number of linkers in as-synthesized and thermally treated samples by quantifying carbon dioxide from the combustion of the ABTC linker. The materials were heated at 0.05 K s<sup>-1</sup> starting from 423 K in 0.83 cm<sup>3</sup> s<sup>-1</sup> He,  $0.17 \text{ cm}^3 \text{ s}^{-1} \text{ Ar}$ , and  $0.17 \text{ cm}^3 \text{ s}^{-1} \text{ O}_2$  until 723 K. The thermally treated sample (493 K in 0.83 cm<sup>3</sup> s<sup>-1</sup> for 4 h) was cooled to 423 K before ramping the temperature at 0.05 K s<sup>-1</sup>. As depicted in Figure 2a, carbon dioxide is observed at temperatures >523 K, consistent with the thermal stability of MIL-127-type materials.<sup>34</sup> The amount of CO<sub>2</sub> can be quantified by integration of the flow rate of CO2 over the time duration when CO<sub>2</sub> is observed in the effluent, and this amount of CO2 can be normalized by the mass of the material to determine 28.7  $\pm$  3.7 and 22.4  $\pm$  4.0 mmol  $g_{cat}^{-1}$  of  $CO_2$ evolved for the as-synthesized and thermally treated samples, respectively. Based on the stoichiometry of the ABTC linker, there are 16 carbon atoms per organic linker, and there are  $1.79 \pm 0.23$  and  $1.40 \pm 0.25$  mmol  $g_{cat}^{-1}$  of organic linkers in as-synthesized and thermally treated samples, respectively. From TPO, ~22% of linkers are lost upon thermal treatment.

In conjunction with TPO, we show in Figure 2b the <sup>1</sup>H NMR spectra for the digested as-synthesized (black) and thermally treated (red) Ni-MIL-127 in a 1 M solution of  $NH_4OH/D_2O$  with 100  $\mu L$  of acetonitrile as the internal standard. The ABTC linker (8.53 ppm) intensities are normalized by the amount of Ni-MIL-127 and the intensity of the internal standard. The chemical shift for the ABTC linker was verified using the pure linker dissolved in NH4OH/ D<sub>2</sub>O (Figure S4). The number of organic linkers in the assynthesized and thermally treated Ni-MIL-127 was 2.14 mmol  $g_{cat}^{-1}$  and 1.69 mmol  $g_{cat}^{-1}$ , respectively, as assessed by integration of NMR peaks. This indicates that  $\sim$ 22% of the linkers are lost upon thermal treatment, consistent with our observations from TPO. We attribute a lower absolute value of linkers determined by TPO compared to <sup>1</sup>H NMR to plausible incomplete combustion of the ABTC linker, where aromatic fragments (m/z = 78) are observed (Figure S9). The TPO data reported in Figures 1a and S4-S7 for the as-synthesized and thermally activated Ni-MIL-127 species do not have observable aromatic fragments, but we cannot eliminate the possibility of aromatic fragments being formed during TPO due to incomplete combustion of Ni-MIL-127. Nevertheless, a decrease in carbon content and ABTC linkers of 22% is observed from TPO and <sup>1</sup>H NMR, respectively, to suggest that linkers are removed from the MOF during thermal treatment.

The stability of the material with the incorporation of defects can be verified with PXRD and  $N_2$  isotherms (Figure 1b and 1c, respectively), where the material maintains

crystallinity and porosity.  $^{1,35}$  After degassing the sample at 393 and 493 K for 4 h in vacuum (<100 Pa), a BET surface area of 1003 and 1551 m<sup>2</sup> g<sup>-1</sup>, respectively, is observed (Table S1). This increase in surface area is proposed to be positively correlated with defectivity in MOF materials as seen in UiO-66 and MOF-74 and is consistent with our observations that missing linker defects are engendered upon thermal treatment.  $^{12,36}$ 

XAS was used to explore the effect of missing linker defects on the nickel active sites on Ni-MIL-127. Comparing the X-ray absorption near-edge structure (XANES) data between the assynthesized and thermally treated sample at 513 K in helium (Figure 2c), minimal changes in the absorption edge energies are observed, but variations in the XANES spectra for the assynthesized and thermally treated samples show an increase in the pre-edge shoulder at 8440 eV, a decrease in the white line intensity, and subtle changes in the post edge XANES spectra for the thermally treated samples. The latter corresponds to changes in the extended X-ray absorption fine structure (EXAFS) spectra for the two states, where a decrease in the amplitude of the oscillations in the EXAFS spectra (Figure S31) and a decrease in the overall magnitude of the first scattering contribution in the Fourier transform of the EXAFS spectrum (Figure 2d) is observed when comparing the transformation between the as-synthesized and thermally treated samples. The pre-edge feature at 8440 eV (inset of Figure 2c) in the thermally treated sample is attributed to a 1s to 4pz transition, consistent with the 5-coordinate square pyramidal configuration of Ni which arises due to symmetry reduction and a decrease in the inversion center symmetry. 37-39 From EXAFS fitting of the first coordination shell in Figure 2d to a Ni-O scattering path, a decrease in the Ni-O coordination from  $6.0 \pm 0.6$  to  $5.3 \pm 0.7$  for the as-synthesized and thermally treated samples (see Section S5), respectively, is determined, which suggests an increase in the number of uncoordinated nickel species in the thermally treated samples. This decrease in Ni-O coordination is consistent with the formation of the 5-coordinate signature at 8440 eV (inset of Figure 2c). The decrease in the white line intensity and amplitude of the oscillations in the post edge XANES spectrum are likely due to the removal of the ABTC ligands. These XAS results corroborate a decrease in nickel coordination to generate an open coordination site through a missing linker defect, as shown from TPO and <sup>1</sup>H NMR results, to facilitate propylene oligomerization on Ni-MIL-127.

Our goal was to determine the structure of the assynthesized and thermally treated Ni-MIL-127 materials from TPO, <sup>1</sup>H NMR, and XAS. We examined the plausibility of the formation of the activated material using DFT on cluster models with benzene-capped linkers of Ni-MIL-127 as

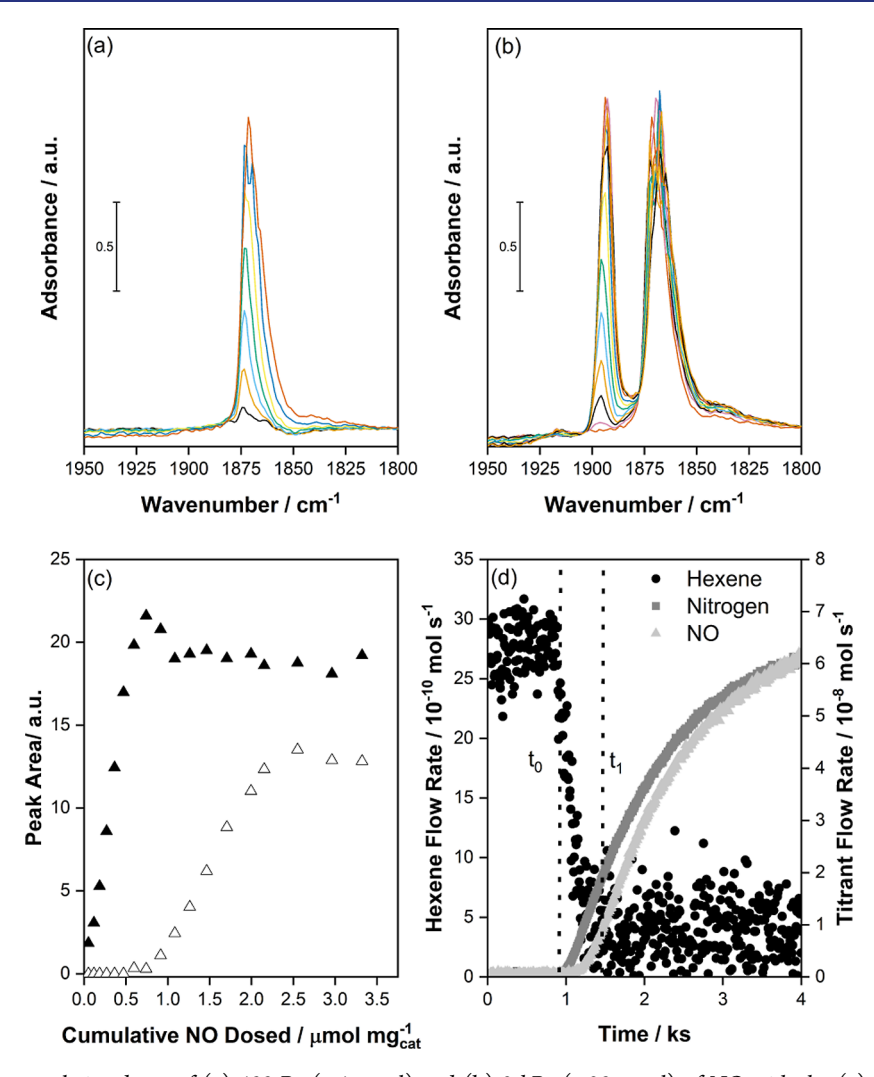


Figure 3. IR spectra with cumulative doses of (a) 400 Pa ( $\sim$ 4  $\mu$ mol) and (b) 2 kPa ( $\sim$ 20  $\mu$ mol) of NO with the (c) corresponding plot of the integration of the Ni(II)–NO ( $\triangle$ ) and Fe(III)–NO ( $\triangle$ ) band areas vs the cumulative amount of NO dosed on 7.7 mg of as-synthesized Ni-MIL-127 at 77 K. (d) In situ NO titration showing a decrease in the rate of hexene formation ( $\bullet$ ) upon introduction of 0.17 cm<sup>3</sup> s<sup>-1</sup> of 1% NO ( $\triangle$  gray) and 99% N<sub>2</sub> ( $\blacksquare$ ) in 0.83 cm<sup>3</sup> s<sup>-1</sup> at a total pressure of 500 kPa at 493 K on 29.8 mg of Ni-MIL-127.

opposed to those with formate-capped linkers proposed by Barona et al. 40 We propose that nickel on the as-synthesized Ni-MIL-127 structure contains four ABTC linkers, one bridging oxo species, and one water molecule as determined from our best fit EXAFS model (Scheme 1). Based upon our analysis of the material upon thermal treatment where a missing linker defect is generated as shown by TPO and <sup>1</sup>H NMR (Figure 2a and 2b), and no change in the formal charge of the nickel is noted from XANES spectra (Figure 2c), we surmise that upon thermal treatment, nickel is bound to three ABTC linkers, a bridging oxo species, and an OH<sup>-</sup> ligand to maintain the oxidation state of nickel (Scheme 1). Using DFT, the generation of this missing linker defect and the unsaturated Ni-MIL-127 species yields a change in free energy of 82 kJ mol<sup>-1</sup> at 298 K with respect to the as-synthesized Ni-MIL-127 material. However, at the pretreatment temperature of 493 K, the change in free energy to generate the missing linker defect is 25 kJ mol<sup>-1</sup>. This decrease in free energy is consistent with our observations that it is more favorable to form missing linker defects at higher temperatures.

The effect of missing linker defects, which engender a coordinately unsaturated nickel site on Ni-MIL-127 for

oligomerization catalysis, was evaluated by running propylene oligomerization at 433 K and 500 kPa of 0.83 cm<sup>3</sup> s<sup>-1</sup> of propylene before and after thermal activation in helium at 493 K in  $0.83 \text{ cm}^3 \text{ s}^{-1}$ , as shown in Figure S16. Without prior thermal activation, propylene oligomerization rates decrease with time on stream. After thermally treating Ni-MIL-127 at 493 K, a ~4× enhancement in rate is observed at the same reaction conditions, and the catalyst maintains stable propylene oligomerization rates. Thus, we surmise that these missing linker defects are necessary for olefin oligomerization stability in MOFs, as previous work for ethylene and butene dimerization on Ni/UiO-66, a MOF with inherent missing linker defects, shows stable oligomerization rates, <sup>22,32</sup> while Ni-MOF-74, a MOF that does not have missing linker defects, deactivates with time on stream for propylene oligomerization.<sup>28,37</sup> The stability of Ni-MIL-127 for propylene oligomerization is unique and allows us to probe and enumerate the relevant active sites, measure steady-state kinetics and product selectivities, and scrutinize reaction mechanisms for propylene oligomerization.

Accessible nickel sites on Ni-MIL-127, generated upon removing linkers, which catalyze propylene oligomerization

Scheme 2. Initiation Mechanism and Cossee-Arlman Mechanism for Propylene Oligomerization on Ni-MIL-127

# Initiation Mechanism Oww.Ni WH В $BC_{TS}$ **EF**<sub>TS</sub> Cossee-Arlman Mechanism C Ε DETS D

were enumerated using NO titrations ex situ and in situ. The upper bound estimate of nickel active sites was determined ex situ using low-temperature (77 K) infrared (IR) dosing experiments with NO. In Figure 3a and 3b, we show the IR spectra of an as-synthesized sample after dosing 400 Pa (~4  $\mu$ mol) and 2 kPa (~20  $\mu$ mol) of NO on 7.7 mg of Ni-MIL-127. At low NO pressures, we observe a band at 1873 cm<sup>-1</sup> attributed to Ni(II)–NO.<sup>31</sup> Upon subsequent NO dosing, the Ni(II)-NO band saturates, and another band appears at 1894 cm<sup>-1</sup>. This band at 1894 cm<sup>-1</sup> corresponds to a Fe(III)-NO species, which is consistent with the IR frequencies of Fe(III)— NO bands for as-synthesized MIL-127-type materials at subambient temperatures <sup>31,41,42</sup> and the oxidation state of the Fe species determined by Mössbauer spectroscopy at 25 K (Figure S3). The amount of nickel and iron was quantified by integration of band areas upon NO dosing until the bands saturated, as depicted in Figure 3c. The Ni(II)-NO and Fe(III)-NO bands saturate after dosing 595  $\mu$ mol  $g_{cat}^{-1}$  and a subsequent 1557  $\mu$ mol  $g_{cat}^{-1}$ , respectively, a cumulative NO dose of ~2152  $\mu$ mol  $g_{cat}^{-1}$ . This yields a Ni/Fe ratio of 1:2.6, consistent with the Ni/Fe ratio obtained from EDS (Table S1, eq S2).

Previous work has reported that various nickel moieties exist and only (Ni-OH)<sup>+</sup> species are active for propylene

oligomerization on Ni-Al-MCM-41 at 248 K and 230 kPa.<sup>23,24</sup> Similar observations in MOF systems have been made, where not all Ni species are active during ethylene oligomerization in Ni/UiO-66.<sup>22</sup> Thus, we aimed to enumerate the active sites in situ during propylene oligomerization as shown in Figure 3d to accurately normalize reaction rates. Once propylene oligomerizations rates on Ni-MIL-127 reached a steady state at 500 kPa and 493 K, a mixture of 1% NO and 99% N<sub>2</sub> was introduced into the propylene feed, and subsequently, a decrease in the rate of hexene formation was observed. At  $t_0$ , nitrogen achieves breakthrough before NO as NO titrates nickel active sites and impedes the formation of hexene until  $t_1$ . We note that NO continues to have a delayed breakthrough response even after hexene is no longer formed after  $t_1$  as NO titrates the iron in the MOF after nickel is titrated. This phenomenon is consistent with the ex situ IR data for the as-synthesized material presented in Figure 3c, where NO titrates nickel active sites before iron. As shown in Figure S13, the pure iron analogue of Ni-MIL-127 is inactive for propylene oligomerization, and thus, we attribute the decrease in hexene formation to the loss of nickel active sites. The amount of active nickel is quantified by numerical integration between the normalized nitrogen and NO 

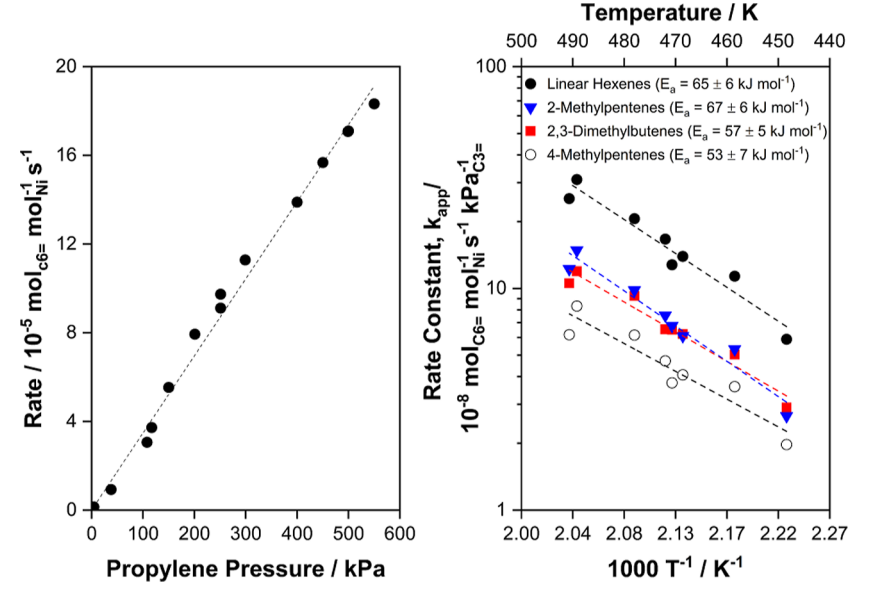


Figure 4. (a) Hexene formation rate vs propylene partial pressure (5–550 kPa) at 473 K on Ni-MIL-127. (b) Arrhenius plot for propylene oligomerization to form linear hexenes (●), 2-methylpentenes (▼ blue), 2,3-dimethylbutenes (■ red), and 4-methylpentenes (○) at 500 kPa from 448 to 493 K for Ni-MIL-127.

bound  $371 \pm 18 \ \mu \text{mol g}_{\text{cat}}^{-1}$  of nickel was obtained at various titration conditions (see Section S4), assuming that one NO molecule binds to one nickel. Comparing the amount of NO adsorbed ex situ on as-synthesized samples (Figure 3c) and the uptake of NO in in situ titration experiments to impede hexene formation (Figure 3d),  $\sim$ 62% of nickel atoms are active for propylene oligomerization, consistent with the degree of coordination fitted from EXAFS, where  $\sim$ 70% of nickel atoms have an open coordination site (Figure 2d; Table S9).

Propylene Oligomerization Reaction Mechanism and **Kinetics.** The Ni-MIL-127 precatalyst after thermal activation undergoes an induction period, as shown in Figure 1d, to generate the relevant surface Ni species for propylene oligomerization. We propose that the initiation mechanism for propylene oligomerization (Scheme 2) consists of a series of stoichiometric reactions of propylene to form hexadiene and water which facilitates the formation of a Ni-hydride or Nipropyl species, similar to the initiation mechanism presented for ethylene and butene oligomerization. <sup>18,21,32</sup> In Figure S14, an increase in propylene pressure from 114 to 500 kPa decreases the induction period from ~170 to ~60 ks at 473 K, consistent with previous observations where higher ethylene pressures decrease the duration of the induction period for ethylene oligomerization on Ni/UiO-66.<sup>22</sup> Additionally, an increase in reaction temperature from 473 to 513 K decreases the induction period from ~170 to ~30 ks at 114 kPa, congruous with observations on Ni-Na-X where activating the catalyst at 493 K eliminates the induction period that was observed at 453 K.<sup>26</sup> Hexadiene formation (Figure S15) is also detected during the induction period at 500 kPa and 473 K. These observations imply propylene pressures and reaction temperatures affect the rate at which relevant surface intermediates are formed prior to a steady state.

The relevant Ni-propyl species formed during the induction period were examined through steady-state kinetics and spectroscopic measurements. Propylene oligomerization is first-order in propylene pressure from 5 to 550 kPa on Ni-MIL-127 at 473 K as shown in Figure 4a. This suggests that

the resting state of the catalyst at a steady state is a Ni-propyl species, considering that two propylene molecules are required to form hexene. The Ni-propyl surface intermediate was probed with IR spectroscopy after the catalyst reached a steady state after exposure to propylene for 2 days (Figure S14) at 473 K and ambient pressure and subsequently degassing the sample (<3 Pa). In Figure S11, aliphatic C-H bands at 2962, 2923, and 2867 cm<sup>-1</sup> are observed,<sup>45</sup> consistent with the presence of a Ni-propyl species that was posited from observed first-order reaction kinetics for propylene oligomerization. Subtle differences in the XANES region are observed between the thermally treated samples and the structure at steady state (Figure 2c), but the pre-edge peak at 8440 eV persists and suggests a five-coordinate nickel species. The EXAFS results for Ni-MIL-127 after thermal treatment and at steady state reported in Figure S31 are similar, and the fitting of the first coordination shell (see Section S5) shows that, within error, Ni maintains the same coordination (Table S9). We note that Ni-C and Ni-O bonds cannot be differentiated, so the loss of an OH<sup>-</sup> species and the formation of a propyl ligand cannot be resolved. However, we surmise that the Ni-OH moiety is removed via migratory insertion of propylene to eliminate water during the induction period 18 and generate the steadystate Ni-propyl species (Scheme 2) which justifies similar coordination and geometries between the two structures.

After the relevant Ni-propyl species is formed during the induction period on Ni-MIL-127, olefin oligomerization is proposed in the literature to follow the Cossee–Arlman mechanism on nickel catalysts as presented in Scheme 2. 18,19,29,46–52 Isomers of linear hexenes, 2-methylpentenes, 4-methylpentenes, and 2,3-dimethylbutenes are generated from the Cossee–Arlman cycle by regioselective insertion of adsorbed propylene molecules. Herein, we report the mechanism for the production of linear hexenes, while others are reported in Section S6. The Cossee–Arlman mechanism starts with a nickel–hydride species (A) that binds to a propylene molecule to give a nickel–hydride species with propylene physisorbed on the surface (B). 1,2-Propyl (C) or

2,1-propyl species are formed upon migratory insertion ( $BC_{TS}$ ) of the hydride species and are the relevant surface species. Another propylene molecule is adsorbed on C to generate propylene adsorbed on the Ni-propyl species (D). The kinetically relevant 1,2- and 2,1- olefin insertions ( $DE_{TS}$ ) proceed on **D** to generate isomeric Ni-hexyl species (**E**).<sup>29</sup> The Ni-hexyl species undergo  $\beta$ -hydride elimination (EF<sub>TS</sub>) to yield physisorbed hexene (F) which desorbs to regenerate A and produce the respective hexene isomers.

The validity of the Cossee-Arlman mechanism was investigated by comparison between experimental and computed apparent activation energies. An Arrhenius plot presented in Figure 4b for linear hexenes, 2-methylpentenes, 4methylpentenes, and 2,3-dimethylbutenes reveals apparent activation enthalpies of 65.0  $\pm$  5.8, 67.3  $\pm$  5.9, 53.4  $\pm$  7.2, and  $56.8 \pm 4.8 \text{ kJ} \text{ mol}^{-1}$ , respectively, between 448 and 493 K at 500 kPa on Ni-MIL-127. The measured apparent activation energies for the different hexene isomers are within error of each other as the product selectivities appear to be invariant with temperature (Figure S25). These apparent activation energies are comparable with the activation energies of 58 and 45 kJ mol<sup>-1</sup> on Ni/UiO-66 for butene oligomerization and on Ni-Na-X for propylene oligomerization, respectively. 26,32

The calculated enthalpy and free energy diagrams from DFT with the M06-L functional for linear hexene formation via the Cossee-Arlman mechanism are presented in Figure 5 on

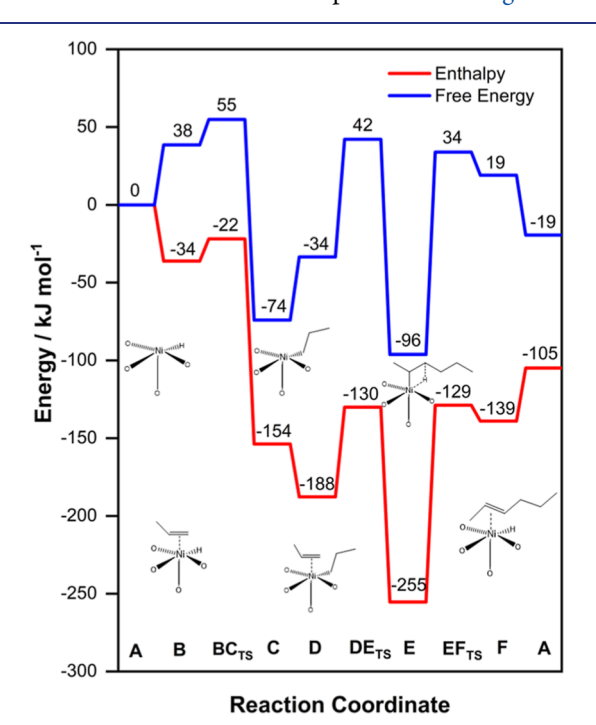


Figure 5. Enthalpy (red) and free energy (blue) diagram for the synthesis of linear hexenes via propylene oligomerization through the Cossee-Arlman mechanism for Ni-MIL-127 at 473 K and 101.3 kPa. Intermediate structures ( $S^2 = 11$ ) are shown along the reaction pathway.

cluster models of Ni-MIL-127 ( $S^2 = 11$ ) at 493 K and 101.3 kPa, while the enthalpy and free energy diagrams for the other hexene isomers are presented in Figures S32-S35. The free energy of adsorbing a propylene molecule to generate B is 38 kJ mol<sup>-1</sup>, akin to ethylene and 1-butene adsorption free energies on Ni/UiO-66 of 17 and 55 kJ mol<sup>-1</sup>, respec-

tively. 22,32 The hydride insertion step (BCTS), olefin insertion step (DE<sub>TS</sub>), and  $\beta$ -hydride elimination step (EF<sub>TS</sub>) yield free energy barriers of 17, 76, and 120 kJ mol<sup>-1</sup>, respectively. The calculated migratory insertion and olefin insertion intrinsic free energies on Ni/UiO-66 for ethylene oligomerization are 22 and 80 kJ mol<sup>-1</sup>, respectively, consistent with the values reported in Figure 5.<sup>22</sup> We note that the barrier for  $\beta$ -hydride elimination of 130 kJ mol<sup>-1</sup> is higher than what is reported for ethylene and butene oligomerization on Ni/UiO-66.22,32 We attribute the larger  $\beta$ -hydride elimination barrier of 130 kJ mol<sup>-1</sup> for linear hexenes due to a combination of the change in the spin state found in the nickel framework-based MOFs<sup>51</sup> and the specific hexene isomer that is produced. Nickelframework-based MOFs, such as Ni-MFU-4l, for olefin oligomerization have been proposed to change spin states along the reaction coordinate <sup>\$1</sup> while olefin oligomerization on nickel-supported MOFs, such as Ni/UiO-66, do not. 22,32,52 Ni-MFU-41 yields higher reaction barriers for  $\beta$ -hydride elimination (72 kJ mol<sup>-1</sup>)<sup>51</sup> compared to  $\beta$ -hydride elimination barrier on Ni/UiO-66 (48 kJ mol-1)for ethylene oligomerization<sup>22</sup> where a change in the triplet to singlet spin state on Ni-MFU-4l along the reaction coordinate was attributed to contribute toward the higher observed barrier on framework-based MOFs for  $\beta$ -hydride elimination. Similarly, a change in spin state is observed for intermediates **E** and **F** on Ni-MIL-127 to give rise to a higher  $\beta$ -hydride elimination barrier (Section S1; Table S11). Additionally, the  $\beta$ -hydride elimination step, which affects whether internal or terminal alkenes are produced, for the Cossee-Arlman mechanism yield intrinsic free energy barriers of ~130 and ~60 kJ mol<sup>-1</sup> for internal and terminal alkenes, respectively (Figures 5 and S35–S38). The higher  $\beta$ -hydride elimination barrier of 130 kJ mol<sup>-1</sup> for 2-hexene presented herein can be ascribed to a change in the spin state for this step and the specific structural hexene isomer formed.

Because of the first-order kinetics observed in experimental studies (Figure 4a), the resting state of the catalyst is likely the Ni-propyl species (C). The kinetically relevant step for the formation of hexenes from C is the olefin insertion step (DE<sub>TS</sub>) as the apparent free energy barrier is 116 kJ mol<sup>-1</sup> as opposed to 108 kJ mol<sup>-1</sup> for the  $\beta$ -hydride elimination step (EF<sub>TS</sub>). From the kinetically relevant olefin insertion step (DE<sub>TS</sub>) and the most relevant surface Ni-propyl species (C) determined from steady-state reaction orders and IR and XAS spectroscopy, we obtain calculated apparent activation enthalpies for linear hexenes, 2-methylpentenes, 4-methylpentenes, and 2,3-dimethylbutenes in the range of 24-42 kJ mol<sup>-1</sup> (Figures S32-S35), somewhat lower than the apparent activation energies of ~53-65 kJ mol<sup>-1</sup> obtained from experiment. These values are within the  $8{\text -}23~\text{kJ}~\text{mol}^{-1}$  error of DFT using the M06-L functional and are consistent with errors found in olefin oligomerization on Ni/UiO-66 and Ni/ NU-1000 MOF materials. 22,32,52

Metallacycle and proton-transfer mechanisms for propylene oligomerization were investigated as alternatives to the Cossee—Arlman mechanism by comparison of expected trends for these alternative mechanisms with experimental observations and by comparison of DFT computed energy barriers for all three mechanisms (Section S8). 18,53 The metallacycle mechanism (Scheme S7) on nickel catalysts is characteristic of external activators, successive coordination of two olefin molecules, and a redox reaction on the nickel active site. 18,19,54,55 The observed induction period in the absence

of activators, the five-coordinate nickel species after thermal treatment (Table S9) that is unable to directly coordinate two propylene molecules, and a persistent Ni(II) species after thermal treatment and during the reaction as indicated by XANES (Figure 2c) are incongruous with the metallacycle mechanism for propylene oligomerization on Ni-MIL-127. The proton-transfer pathway was scrutinized with DFT calculations (Section S8, Scheme S6, and Figure S40), where the C-H activation step was found to be the kinetically relevant step in our work and previous studies for ethylene oligomerization on Ni-SSZ-24 and 1-butene oligomerization on Ni/UiO-66. 18,32,53 The intrinsic free energy barrier for the rate-limiting C-H step of 191 kJ mol<sup>-1</sup> for the proton-transfer mechanism (Figure S40) is higher than the intrinsic free energy for the kinetically relevant carbon-carbon coupling step of 76 kJ mol<sup>-1</sup> for the Cossee-Arlman mechanism (Figure 5). These observations and calculations render the Cossee-Arlman mechanism most favorable for propylene oligomerization on Ni-MIL-127 compared to the metallacycle and proton-transfer mechanisms. The Ni-MIL-127 structure, initiation mechanism, and Cossee-Arlman mechanism for propylene oligomerization are consistent with our spectroscopic measurements, observed induction periods, and steady-state kinetics.

#### CONCLUSIONS

Thermal treatment on Ni-MIL-127, which contains a fully coordinated nickel atom in the inorganic node, generates a missing linker defect on nickel to engender a five-coordinate nickel site to facilitate stable propylene oligomerization after undergoing an induction period in the absence of cocatalysts and activators. Transient and steady-state rate measurements suggest that the induction period is attributed to the formation of the relevant Ni-propyl species at a steady state. The steady-state Cossee—Arlman mechanism is validated on Ni-MIL-127 for propylene oligomerization by comparison between experimental and computed activation energies. These results demonstrate how the stable Ni-MIL-127 MOF reported herein can be designed to further improve the reactivity for olefin oligomerization through a synergy between experiment and theory.

#### ASSOCIATED CONTENT

#### Supporting Information

The Supporting Information is available free of charge at https://pubs.acs.org/doi/10.1021/jacs.2c10551.

Ni-MIL-127 C3 oligomerization, experimental and computational details, material characterization and synthesis, catalysis, density functional theory calculations, and DFT coordinates (PDF)

xyz coordinates of computational models (ZIP)

#### AUTHOR INFORMATION

#### **Corresponding Author**

Aditya Bhan — Department of Chemical Engineering and Materials Science, University of Minnesota-Twin Cities, Minneapolis, Minnesota 55455, United States; oorcid.org/0000-0002-6069-7626; Email: abhan@umn.edu

#### **Authors**

Benjamin Yeh – Department of Chemical Engineering and Materials Science, University of Minnesota-Twin Cities, Minneapolis, Minnesota 55455, United States

- Saumil Chheda Department of Chemical Engineering and Materials Science, University of Minnesota-Twin Cities, Minneapolis, Minnesota 55455, United States; Department of Chemistry, Chemical Theory Center, and Supercomputing Institute, University of Minnesota-Twin Cities, Minneapolis, Minnesota 55455, United States
- Steven D. Prinslow Department of Chemistry, Chemical Theory Center, and Supercomputing Institute, University of Minnesota-Twin Cities, Minneapolis, Minnesota 55455, United States
- Adam S. Hoffman Stanford Synchrotron Radiation Lightsource, SLAC National Accelerator Laboratory, Menlo Park, California 94025, United States; oocid.org/0000-0002-7682-4108
- Jiyun Hong Stanford Synchrotron Radiation Lightsource, SLAC National Accelerator Laboratory, Menlo Park, California 94025, United States
- Jorge E. Perez-Aguilar Stanford Synchrotron Radiation Lightsource, SLAC National Accelerator Laboratory, Menlo Park, California 94025, United States
- Simon R. Bare Stanford Synchrotron Radiation Lightsource, SLAC National Accelerator Laboratory, Menlo Park, California 94025, United States
- Connie C. Lu Department of Chemistry, Chemical Theory Center, and Supercomputing Institute, University of Minnesota-Twin Cities, Minneapolis, Minnesota 55455, United States; Present Address: Institut für Anorganische Chemie, Rheinische-Friedrich-Wilhelms-Universität Bonn, Gerhard-Domagk-Strasse 1, 53121 Bonn, Germany; orcid.org/0000-0002-5162-9250
- Laura Gagliardi Department of Chemistry, The University of Chicago, Chicago, Illinois 60637, United States;
  orcid.org/0000-0001-5227-1396

Complete contact information is available at: https://pubs.acs.org/10.1021/jacs.2c10551

#### Notes

The authors declare no competing financial interest.

#### ACKNOWLEDGMENTS

This work was supported by the Inorganometallic Catalyst Design Center, an Energy Frontier Research Center, which is funded by the US Department of Energy (DOE), Office of Science, Basic Energy Sciences (BES) (DE-SC0012702). B.Y. acknowledges the National Science Foundation for a graduate research fellowship and a departmental fellowship funded by 3M. The authors acknowledge the Minnesota Supercomputing Institute (MSI) at the University of Minnesota for providing computational resources for this research. PXRD and SEM-EDS were carried out in the Characterization Facility, University of Minnesota, which receives partial support from the National Science Foundation (NSF) through the MRSEC program, with help from Dr. Xinyu Li and Brian Bayer, respectively. Mössbauer spectroscopy was performed at the Institute for Rock Magnetism (IRM) at the University of Minnesota with the help of Peter Solheid. The IRM is a US National Multiuser Facility supported through the Instrumentation and Facilities program of the NSF, Earth Sciences Division, and by funding from the University of Minnesota. Research reported in this publication was supported by the Office of the Director, National Institutes of Health, under Award Number S10OD011952. The content is solely the

responsibility of the authors and does not necessarily represent the official views of the National Institutes of Health. Part of this work was performed at the Stanford Synchrotron Radiation Lightsource (SSRL) of SLAC National Accelerator Laboratory by Co-ACCESS, supported by the US Department of Energy, Office of Basic Energy Sciences, Chemical Sciences, Geosciences, and Biosciences Division. We thank Professor Omar Farha, Dr. Madhuresh Choudhary, Dr. Matthew Simons, Dr. Zhichen Shi, Dr. Neil Razdan, Ting Lin, Matthew Jacob, and Joseph Esposito for helpful technical discussions.

#### REFERENCES

- (1) Yang, D.; Gates, B. C. Catalysis by Metal Organic Frameworks: Perspective and Suggestions for Future Research. *ACS Catal.* **2019**, *9*, 1779–1798.
- (2) Canivet, J.; Vandichel, M.; Farrusseng, D. Origin of Highly Active Metal-Organic Framework Catalysts: Defects? Defects! *Dalton Trans.* **2016**, *45*, 4090–4099.
- (3) Sholl, D. S.; Lively, R. P. Defects in Metal-Organic Frameworks: Challenge or Opportunity? *J. Phys. Chem. Lett.* **2015**, *6*, 3437–3444.
- (4) Hall, J. N.; Bollini, P. Structure, Characterization, and Catalytic Properties of Open-Metal Sites in Metal Organic Frameworks. *React. Chem. Eng.* **2019**, *4*, 207–222.
- (5) Kirchon, A.; Feng, L.; Drake, H. F.; Joseph, E. A.; Zhou, H. C. From Fundamentals to Applications: A Toolbox for Robust and Multifunctional MOF Materials. *Chem. Soc. Rev.* **2018**, 47, 8611–8638
- (6) Liu, S.; Zhang, Y.; Han, Y.; Feng, G.; Gao, F.; Wang, H.; Qiu, P. Selective Ethylene Oligomerization with Chromium-Based Metal-Organic Framework MIL-100 Evacuated under Different Temperatures. *Organometallics* 2017, 36, 632–638.
- (7) Drake, H. F.; Day, G. S.; Vali, S. W.; Xiao, Z.; Banerjee, S.; Li, J.; Joseph, E. A.; Kuszynski, J. E.; Perry, Z. T.; Kirchon, A.; et al. The Thermally Induced Decarboxylation Mechanism of a Mixed-Oxidation State Carboxylate-Based Iron Metal-Organic Framework. *Chem. Commun.* **2019**, *55*, 12769–12772.
- (8) Vermoortele, F.; Bueken, B.; Le Bars, G.; Van de Voorde, B.; Vandichel, M.; Houthoofd, K.; Vimont, A.; Daturi, M.; Waroquier, M.; Van Speybroeck, V.; et al. Synthesis Modulation as a Tool to Increase the Catalytic Activity of Metal-Organic Frameworks: The Unique Case of UiO-66(Zr). *J. Am. Chem. Soc.* **2013**, *135*, 11465–11468.
- (9) Vermoortele, F.; Vandichel, M.; Van de Voorde, B.; Ameloot, R.; Waroquier, M.; Van Speybroeck, V.; De Vos, D. E. Electronic Effects of Linker Substitution on Lewis Acid Catalysis with Metal-Organic Frameworks. *Angew. Chem., Int. Ed.* **2012**, *51*, 4887–4890.
- (10) Liu, Y.; Klet, R. C.; Hupp, J. T.; Farha, O. Probing the Correlations between the Defects in Metal-Organic Frameworks and Their Catalytic Activity by an Epoxide Ring-Opening Reaction. *Chem. Commun.* **2016**, *52*, 7806–7809.
- (11) Valenzano, L.; Civalleri, B.; Chavan, S.; Bordiga, S.; Nilsen, M. H.; Jakobsen, S.; Lillerud, K. P.; Lamberti, C. Disclosing the Complex Structure of UiO-66 Metal Organic Framework: A Synergic Combination of Experiment and Theory. *Chem. Mater.* **2011**, *23*, 1700–1718.
- (12) Shearer, G. C.; Chavan, S.; Bordiga, S.; Svelle, S.; Olsbye, U.; Lillerud, K. P. Defect Engineering: Tuning the Porosity and Composition of the Metal-Organic Framework UiO-66 via Modulated Synthesis. *Chem. Mater.* **2016**, 28, 3749–3761.
- (13) Gadipelli, S.; Guo, Z. Postsynthesis Annealing of MOF-5 Remarkably Enhances the Framework Structural Stability and CO2 Uptake. *Chem. Mater.* **2014**, *26*, 6333–6338.
- (14) Simons, M. C.; Vitillo, J. G.; Babucci, M.; Hoffman, A. S.; Boubnov, A.; Beauvais, M. L.; Chen, Z.; Cramer, C. J.; Chapman, K. W.; Bare, S. R.; et al. Structure, Dynamics, and Reactivity for Light Alkane Oxidation of Fe(II) Sites Situated in the Nodes of a Metal-Organic Framework. *J. Am. Chem. Soc.* **2019**, *141*, 18142–18151.

- (15) Simons, M. C.; Prinslow, S. D.; Babucci, M.; Hoffman, A. S.; Hong, J.; Vitillo, J. G.; Bare, S. R.; Gates, B. C.; Lu, C. C.; Gagliardi, L.; et al. Beyond Radical Rebound: Methane Oxidation to Methanol Catalyzed by Iron Species in Metal-Organic Framework Nodes. *J. Am. Chem. Soc.* **2021**, *143*, 12165–12174.
- (16) Yang, D.; Bernales, V.; Islamoglu, T.; Farha, O. K.; Hupp, J. T.; Cramer, C. J.; Gagliardi, L.; Gates, B. C. Tuning the Surface Chemistry of Metal Organic Framework Nodes: Proton Topology of the Metal-Oxide-Like Zr6 Nodes of UiO-66 and NU-1000. *J. Am. Chem. Soc.* **2016**, *138*, 15189–15196.
- (17) Henry, R.; Komurcu, M.; Ganjkhanlou, Y.; Brogaard, R. Y.; Lu, L.; Jens, K.-J.; Berlier, G.; Olsbye, U. Ethene Oligomerization on Nickel Microporous and Mesoporous-Supported Catalysts: Investigation of the Active Sites. *Catal. Today* **2018**, *299*, 154–163.
- (18) Brogaard, R. Y.; Olsbye, U. Ethene Oligomerization in Ni-Containing Zeolites: Theoretical Discrimination of Reaction Mechanisms. ACS Catal. 2016, 6, 1205–1214.
- (19) Joshi, R.; Zhang, G.; Miller, J. T.; Gounder, R. Evidence for the Coordination-Insertion Mechanism of Ethene Dimerization at Nickel Cations Exchanged onto Beta Molecular Sieves. *ACS Catal.* **2018**, *8*, 11407–11422.
- (20) Joshi, R.; Saxena, A.; Gounder, R. Mechanistic Insights into Alkene Chain Growth Reactions Catalyzed by Nickel Active Sites on Ordered Microporous and Mesoporous Supports. *Catal. Sci. Technol.* **2020**, *10*, 7101–7123.
- (21) Brogaard, R. Y.; Kømurcu, M.; Dyballa, M. M.; Botan, A.; Van Speybroeck, V.; Olsbye, U.; De Wispelaere, K. Ethene Dimerization on Zeolite-Hosted Ni Ions: Reversible Mobilization of the Active Site. *ACS Catal.* **2019**, *9*, 5645–5650.
- (22) Yeh, B.; Vicchio, S. P.; Chheda, S.; Zheng, J.; Schmid, J.; Löbbert, L.; Bermejo-Deval, R.; Gutiérrez, O. Y.; Lercher, J. A.; Lu, C. C.; et al. Site Densities, Rates, and Mechanism of Stable Ni/UiO-66 Ethylene Oligomerization Catalysts. *J. Am. Chem. Soc.* **2021**, *143*, 20274–20280.
- (23) Agirrezabal-Telleria, I.; Iglesia, E. Mechanistic Insights and Consequences of Intrapore Liquids in Ethene, Propene, and Butene Dimerization on Isolated Ni2+ Sites Grafted within Aluminosilicate Mesopores. *J. Catal.* **2020**, 389, 690–705.
- (24) Agirrezabal-Telleria, I.; Iglesia, E. Stabilization of Active, Selective, and Regenerable Ni-Based Dimerization Catalysts by Condensation of Ethene Withinordered Mesopores. *J. Catal.* **2017**, 352, 505–514.
- (25) Keim, W. Oligomerization of Ethylene to  $\alpha$ -Olefins: Discovery and Development of the Shell Higher Olefin Process (SHOP). *Angew. Chem., Int. Ed.* **2013**, *52*, 12492–12496.
- (26) Mlinar, A. N.; Baur, G. B.; Bong, G. G.; Getsoian, A.; Bell, A. T. Propene Oligomerization over Ni-Exchanged Na-X Zeolites. *J. Catal.* **2012**, *296*, 156–164.
- (27) Mlinar, A. N.; Shylesh, S.; Ho, O. C.; Bell, A. T. Propene Oligomerization Using Alkali Metal- and Nickel-Exchanged Mesoporous Aluminosilicate Catalysts. *ACS Catal.* **2014**, *4*, 337–343.
- (28) Mlinar, A. N.; Keitz, B. K.; Gygi, D.; Bloch, E. D.; Long, J. R.; Bell, A. T. Selective Propene Oligomerization with Nickel(II)-Based Metal-Organic Frameworks. *ACS Catal.* **2014**, *4*, 717–721.
- (29) Comito, R. J.; Metzger, E. D.; Wu, Z.; Zhang, G.; Hendon, C. H.; Miller, J. T.; Dincă, M. Selective Dimerization of Propylene with Ni-MFU-4l. *Organometallics* **2017**, *36*, 1681–1683.
- (30) Feng, D.; Wang, K.; Wei, Z.; Chen, Y. P.; Simon, C. M.; Arvapally, R. K.; Martin, R. L.; Bosch, M.; Liu, T. F.; Fordham, S.; et al. Kinetically Tuned Dimensional Augmentation as a Versatile Synthetic Route towards Robust Metal-Organic Frameworks. *Nat. Commun.* **2014**, *5*, 5723.
- (31) Wongsakulphasatch, S.; Nouar, F.; Rodriguez, J.; Scott, L.; Guillouzer, C. L.; Devic, T.; Horcajada, P.; Greneche, J.-M.; Llewellyn, P. L.; Vimont, A.; et al. Direct Accessibility of Mixed-Metal (III/II) Acid Sites through the Rational Synthesis of Porous Metal Carboxylates. *Chem. Commun.* **2015**, *51*, 10194–10197.
- (32) Zheng, J.; Löbbert, L.; Chheda, S.; Khetrapal, N.; Schmid, J.; Gaggioli, C.; Yeh, B.; Bermejo-Deval, R.; Motkuri, R.;

- Balasubramanian, M.; et al. Metal-Organic Framework Supported Single-Site Nickel Catalysts for Butene Dimerization. *J. Catal.* **2022**, *413*, 176–183.
- (33) Drake, H. F.; Xiao, Z.; Day, G. S.; Vali, S. W.; Chen, W.; Wang, Q.; Huang, Y.; Yan, T. H.; Kuszynski, J. E.; Lindahl, P. A.; et al. Thermal Decarboxylation for the Generation of Hierarchical Porosity in Isostructural Metal-Organic Frameworks Containing Open Metal Sites. *Mater. Adv.* **2021**, *2*, 5487–5493.
- (34) Chevreau, H.; Permyakova, A.; Nouar, F.; Fabry, P.; Livage, C.; Ragon, F.; Garcia-Marquez, A.; Devic, T.; Steunou, N.; Serre, C.; et al. Synthesis of the Biocompatible and Highly Stable MIL-127(Fe): From Large Scale Synthesis to Particle Size Control. *CrystEngComm* **2016**, *18*, 4094–4101.
- (35) Atzori, C.; Shearer, G. C.; Maschio, L.; Civalleri, B.; Bonino, F.; Lamberti, C.; Svelle, S.; Lillerud, K. P.; Bordiga, S. Effect of Benzoic Acid as a Modulator in the Structure of UiO-66: An Experimental and Computational Study. *J. Phys. Chem. C* **2017**, *121*, 9312–9324.
- (36) Wu, D.; Yan, W.; Xu, H.; Zhang, E.; Li, Q. Defect Engineering of Mn-Based MOFs with Rod-Shaped Building Units by Organic Linker Fragmentation. *Inorg. Chim. Acta.* **2017**, 460, 93–98.
- (37) Bonino, F.; Chavan, S.; Vitillo, J. G.; Groppo, E.; Agostini, G.; Lamberti, C.; Dietzel, P. D. C.; Prestipino, C.; Bordiga, S. Local Structure of CPO-27-Ni Metallorganic Framework upon Dehydration and Coordination of NO. *Chem. Mater.* **2008**, *20*, 4957–4968.
- (38) Colpas, G. J.; Maroney, M. J.; Bagyinka, C.; Kumar, M.; Willis, W. S.; Suib, S. L.; Mascharak, N.; Baidya, P. K. X-Ray Spectroscopic Studies of Nickel Complexes, with Application to the Structure of Nickel Sites in Hydrogenases. *Inorg. Chem.* **1991**, *30*, 920–928.
- (39) Alwis, K. H. K. L.; Ingham, B.; Mucalo, M. R.; Kappen, P.; Glover, C. An X-Ray Absorption Spectroscopy Investigation of the Coordination Environment of Electrogenerated Ni(Ii)-Pseudohalide Complexes Arising from the Anodic Polarization of Ni Electrodes in DMSO Solutions of NCO-, NCS- and NCSe- Ions. *RSC Adv.* **2015**, *5*, 15709–15718.
- (40) Barona, M.; Ahn, S.; Morris, W.; Hoover, W.; Notestein, J. M.; Farha, O. K.; Snurr, R. Q. Computational Predictions and Experimental Validation of Alkane Oxidative Dehydrogenation by Fe2M MOF Nodes. *ACS Catal.* **2020**, *10*, 1460–1469.
- (41) Eubank, J. F.; Wheatley, P. S.; Lebars, G.; McKinlay, A. C.; Leclerc, H.; Horcajada, P.; Daturi, M.; Vimont, A.; Morris, R. E.; Serre, C. Porous, rigid metal(III)-carboxylate metal-organic frameworks for the delivery of nitric oxide. *APL Mater.* **2014**, *2*, 124112.
- (42) Vitillo, J. G.; Gagliardi, L. Thermal Treatment Effect on CO and NO Adsorption on Fe(II) and Fe(III) Species in Fe3O-Based MIL-Type Metal-Organic Frameworks: A Density Functional Theory Study. *Inorg. Chem.* **2021**, *60*, 11813–11824.
- (43) Lee, W. S.; Kumar, A.; Wang, Z.; Bhan, A. Chemical Titration and Transient Kinetic Studies of Site Requirements in Mo2C-Catalyzed Vapor Phase Anisole Hydrodeoxygenation. *ACS Catal.* **2015**, *5*, 4104–4114.
- (44) Afrin, S.; Bollini, P. Beyond Upper Bound Estimates of Active Site Densities in Heterogeneous Catalysis: A Note on the Critical Role of Titrant Pressure. *J. Catal.* **2022**, *413*, 76–80.
- (45) Ehrmaier, A.; Liu, Y.; Peitz, S.; Jentys, A.; Chin, Y. H. C.; Sanchez-Sanchez, M.; Bermejo-Deval, R.; Lercher, J. Dimerization of Linear Butenes on Zeolite-Supported Ni 2+. ACS Catal. 2019, 9, 315–324.
- (46) Metzger, E. D.; Comito, R. J.; Hendon, C. H.; Dincă, M. Mechanism of Single-Site Molecule-like Catalytic Ethylene Dimerization in Ni-MFU-4l. *J. Am. Chem. Soc.* **2017**, *139*, 757–762.
- (47) Metzger, E. D.; Brozek, C. K.; Comito, R. J.; Dincă, M. Selective Dimerization of Ethylene to 1-Butene with a Porous Catalyst. ACS Cent. Sci. 2016, 2, 148–153.
- (48) Ye, J.; Gagliardi, L.; Cramer, C. J.; Truhlar, D. G. Single Ni Atoms and Ni4 Clusters Have Similar Catalytic Activity for Ethylene Dimerization. *J. Catal.* **2017**, 354, 278–286.
- (49) Bernales, V.; Ortuño, M. A.; Truhlar, D. G.; Cramer, C. J.; Gagliardi, L. Computational Design of Functionalized Metal-Organic Framework Nodes for Catalysis. *ACS Cent. Sci.* **2018**, *4*, 5–19.

- (50) Liu, J.; Ye, J.; Li, Z.; Otake, K. I.; Liao, Y.; Peters, A. W.; Noh, H.; Truhlar, D. G.; Gagliardi, L.; Cramer, C. J.; et al. Beyond the Active Site: Tuning the Activity and Selectivity of a Metal-Organic Framework-Supported Ni Catalyst for Ethylene Dimerization. *J. Am. Chem. Soc.* **2018**, *140*, 11174–11178.
- (51) Mancuso, J. L.; Gaggioli, C. A.; Gagliardi, L.; Hendon, C. H. Singlet-to-Triplet Spin Transitions Facilitate Selective 1-Butene Formation during Ethylene Dimerization in Ni(II)-MFU-4 L. J. Phys. Chem. C 2021, 125, 22036—22043.
- (52) Ye, J.; Gagliardi, L.; Cramer, C. J.; Truhlar, D. G. Computational Screening of MOF-Supported Transition Metal Catalysts for Activity and Selectivity in Ethylene Dimerization. *J. Catal.* **2018**, *360*, 160–167.
- (53) Bernales, V.; League, A. B.; Li, Z.; Schweitzer, N. M.; Peters, A. W.; Carlson, R. K.; Hupp, J. T.; Cramer, C. J.; Farha, O. K.; Gagliardi, L. Computationally Guided Discovery of a Catalytic Cobalt-Decorated Metal-Organic Framework for Ethylene Dimerization. *J. Phys. Chem. C* 2016, 120, 23576–23583.
- (54) McGuinness, D. S.; Suttil, J. A.; Gardiner, M. G.; Davies, N. W. Ethylene Oligomerization with Cr-NHC Catalysts: Further Insights into the Extended Metallacycle Mechanism of Chain Growth. *Organometallics* **2008**, *27*, 4238–4247.
- (55) Bryliakov, K. P.; Antonov, A. A. Recent Progress of Transition Metal Based Catalysts for the Selective Dimerization of Ethylene. *J. Organomet. Chem.* **2018**, 867, 55–61.

### **□** Recommended by ACS

Monitoring the Activation of Open Metal Sites in  $[Fe_xM_{3-x}(\mu_3-0)]$  Cluster-Based Metal-Organic Frameworks by Single-Crystal X-ray Diffraction

Wenmiao Chen, Hong-Cai Zhou, et al.

FEBRUARY 15, 2023

JOURNAL OF THE AMERICAN CHEMICAL SOCIETY

DEAD E

Programmed Polarizability Engineering in a Cyclen-Based Cubic Zr(IV) Metal-Organic Framework to Boost Xe/Kr Separation

Wei Gong, Omar K. Farha, et al.

JANUARY 18, 2023

JOURNAL OF THE AMERICAN CHEMICAL SOCIETY

READ 🗹

Reticular Design of Precise Linker Installation into a Zirconium Metal-Organic Framework to Reinforce Hydrolytic Stability

Yongwei Chen, Omar K. Farha, et al.

JANUARY 25, 2023

JOURNAL OF THE AMERICAN CHEMICAL SOCIETY

READ 🗹

Homoleptic Acetylacetonate (acac) and β-Ketoiminate (acnac) Complexes of Uranium

Pablo Waldschmidt, Karsten Meyer, et al.

JANUARY 24, 2023

INORGANIC CHEMISTRY

READ 🗹

Get More Suggestions >